



Cite this: *Nanoscale Adv.*, 2025, 7, 1650

Shape-tailored semiconductor dot-in-rods: optimizing CdS-shell growth for enhanced chiroptical properties *via* the rationalization of the role of temperature and time[†]

Junjie Hao, ^{‡abc} Peizhao Liu, ^{‡ch} Ziming Zhou, ^{‡c} Haochen Liu, ^{‡c} Wei Chen, ^{cdf} Peter Müller-Buschbaum, ^{fg} Jiaji Cheng, ^h Kai Wang, ^c Xiao Wei Sun, ^{*c} Jean-Pierre Delville ^{*b} and Marie-Helene Delville ^{*a}

Colloidal chemistry provides an assortment of synthetic tools for tuning the shape of semiconductor nanocrystals. To fully exploit the shape- and structure-dependent properties of semiconductor nanorods, high-precision control on growth and design is essential. However, achieving this precision is highly challenging due to the high temperatures (>350 °C) and short reaction times (<8 minutes) often required for these reactions. In this study, we performed the first investigation on the impact of temperature and time on the CdS-shell growth of CdSe/CdS quantum rods. Our findings demonstrate that temperature plays a pivotal role in achieving ultra-thin shell dot-in-rods, which are crucial for enhancing chiroptical properties. The two-step process proposed here explains the shell growth of CdSe/CdS dot-in-rods (DRs). It involves finely-tuned isotropic shell growth in the first stage, followed by anisotropic length growth along the [0001] rod axis in the second step. This approach has two advantages: a systematic control of the shell thickness for different aspect ratios (ARs) and batch monodispersity. These DRs, with an ultra-thin CdS shell and a high AR, after modification with $\text{l-}\alpha$ -cysteine molecules, exhibit significant enhancement of their ligand-induced chirality, with circular dichroism (CD) *g*-factor values as high as 10^{-3} .

Received 2nd December 2024
Accepted 21st January 2025

DOI: 10.1039/d4na01003e
rsc.li/nanoscale-advances

^aUniv. Bordeaux, CNRS, Bordeaux INP, ICMCB, UMR 5026, F-33600 Pessac, France.
E-mail: marie-helene.delville@icmcb.cnrs.fr

^bUniv. Bordeaux, CNRS, LOMA, UMR 5798, 33405 Talence, France

^cInstitute of Nanoscience and Applications, Department of Electrical and Electronic Engineering, Southern University of Science and Technology, Shenzhen, 518055, China

^dCollege of Engineering Physics, Shenzhen Technology University, Shenzhen, 518118, China

^eCollege of Integrated Circuits and Optoelectronic Chips, Shenzhen Technology University, Shenzhen, 518118, China

^fTechnical University of Munich, TUM School of Natural Sciences, Department of Physics, Chair for Functional Materials, James-Franck-Str. 1, 85748 Garching, Germany

^gHeinz Maier-Leibnitz Zentrum (MLZ), Technical University of Munich, Lichtenbergstraße 1, 85748 Garching, Germany

^hKey Laboratory for the Green Preparation and Application of Functional Materials, Ministry of Education, School of Materials Science and Engineering, Hubei University, Wuhan, 430062, China

[†] Electronic supplementary information (ESI) available: Fig. S1. (a) UV-vis absorption spectra and (b) PL emission spectra of WZ-CdSe cores ($\lambda_{\text{abs}} = 557$ nm). Fig. S2. TEM images of DRs synthesized at different temperatures using the same CdSe cores. Table S1. Physical properties of CdSe/CdS DRs at different reaction times, with two heating power systems. Working temperature 593 K. Table S2. Physical properties of CdSe/CdS DRs at different

ambient temperatures (CdSe core 3.2 nm). Table S3. Characterizations of the thin shell CdSe/CdS DRs using different sizes of CdSe cores. Fig. S3. UV-vis absorption and PL emission spectra of CdSe cores with different sizes. Fig. S4. UV-vis absorption and PL emission spectra of CdSe/CdS DRs with thin shell multi-colour. (a) DR-16 (green), (b) DR-15 (orange), (c) DR-17 (red), (d) DR-18 (red). Table S4. Physical properties of CdSe/CdS with different shell thicknesses (CdSe core (3.2 nm)). Fig. S5. TEM image of DR-23 with a second over-coating process, the shell thickness is 2.0 nm. Fig. S6. UV-vis absorption and PL emission spectra of CdSe/CdS DRs with different shell thicknesses. Fig. S7. Variation of PL emission spectra of CdSe/CdS DRs with different shell thicknesses. Fig. S8. Images comparing the luminescence before and after the ligand exchange. (a) and (b) the oil phase QDs and DRs in hexane; (c) and (d) the aqueous phase QDs and DRs. Images (a) and (c), under natural light, and (b) and (d) under UV light (365 nm). From left to right: CdSe QDs, and DRs with different aspect ratios (see Table 3 for details). Table S5. The CD anisotropy factors of $\text{l-}\alpha$ -CdSe/CdS DRs with different shell thicknesses (CdSe cores ($D = 3.2$ nm)). Table S6. CD anisotropy factors of $\text{l-}\alpha$ -CdSe/CdS DRs with different shell thicknesses (CdSe cores ($D = 3.2$ nm)). Table S7. CD anisotropy factors of $\text{l-}\alpha$ -CdSe/CdS DRs at different core concentrations (CdSe cores ($D = 3.2$ nm)). Table S8. CD anisotropy factors of $\text{l-}\alpha$ -CdSe/CdS DRs at different core concentrations (CdSe cores ($D = 3.2$ nm)). See DOI: <https://doi.org/10.1039/d4na01003e>

[‡] These authors contributed equally.



1 Introduction

The induction of optical activity in colloidal semiconductor nanocrystals (NCs) is a promising way to expand the list of their properties and to enable their use in stereoselective synthesis,^{1–3} chiral recognition,^{4,5} display devices,^{6,7} biosensing,^{8,9} asymmetric catalysis,¹⁰ and so on.^{11–13} Among these properties, chirality remains at the core of intense research, particularly when dealing with the ground and excited electronic (emissive) states of quantum dots (QDs).^{2,14–17} Gun'ko was among the first to report the circular dichroism (CD) response of CdS QDs capped with chiral molecules.¹⁸ This chirality in QDs arises from mechanisms as different as the use of a chiral shell layer,^{18–21} the presence of chiral dislocations and defects,^{3,22,23} ligand-induced chirality,^{16,24,25} and chiral assemblies.^{2,26–28} Among all these mechanisms, ligand exchange with chiral molecules has driven significant progress not only in producing QDs with uniform size distribution but also in designing their surface chemistry to impart the targeted chemical properties. Circularly polarized luminescence (CPL), the counterpart of CD in terms of emission, has been reported in few studies; only spherical and rod-shaped semiconductor NC samples with chiral-ligand-induced CPL have been reported,^{15,16,29,30} where L- and D-cysteine play a central role in CD and CPL performances. The regulation of these optical phenomena by the CdSe/CdS QD morphologies and sizes has been achieved in recent years,^{17,31,32} showing the importance of the presence and the thinness of the CdS layer on the core surface.³² Indeed, the versatility of inorganic nanocrystals (NCs) has been extended significantly, thanks to the ability to tweak their electronic properties by changing their size and dimensionality (high level of fluorescence anisotropy and enhanced potential for electron–hole separation).^{33–36}

CdSe/CdS dot-in-rods (DRs) are visible light-emitting nanocrystals that form robust systems combining a high degree of monodispersity with bright and narrow photoluminescence.^{37–39} However, although rapid initial progress in their development has resulted in the achievement of DRs with different aspect ratios (ARs) and colors in the visible range,^{40–46} improvements in the control of their morphology at the nanoscale, using conventional fast-injection-based preparations, are still under development. This is especially true for the control of a targeted ultra-thin shell.

Even if such thin shells have a positive influence on the improvement of catalytic performances⁴⁷ and chirality,^{17,24,32} to the best of our knowledge, no investigation so far has directly focused on the synthesis of uniform quantum rods that can combine thin shells with varying ARs. Only a few publications mentioned the control of the DR shell thickness. Bawendi³⁸ used a second over-coating process and focused on DRs with thicker shells to enhance the quantum yield (QY) to nearly 100%. She *et al.*⁴⁸ studied the QYs and photophysical processes by systematically tuning the shell and seed sizes, including the thin shell case, but in fact, both the shell layer and length increased simultaneously. Kim *et al.*⁴⁰ proposed a dual-diameter structure for these semiconductor nanorods exhibiting two

distinctly segmented parts with different diameters and a thicker shell on the CdSe seed. Khon *et al.*⁴⁷ obtained thin-shell DRs by etching a 0.7 nm CdS layer from the CdSe/CdS nanorods, enhancing their catalytic activity more than 3 times compared to the original CdSe/CdS DRs.

Additionally, when considering the impact of shell thickness variation on the chiral properties of CdSe/CdS nanorods, two competing effects should be taken into account: (i) the CdS shell acts as an energy barrier for holes within the CdSe core, potentially hindering their chiral electronic coupling with surface ligands and leading to a decrease in CD signals; (ii) conversely, appropriately designed CdS layers can lower the energy of holes, bringing them closer to the energetic resonance of the Highest Occupied Molecular Orbital (HOMO) of the ligand. This closer alignment enhances the CD responses, as it facilitates stronger interactions between holes and ligands. Therefore, the limitations in chirality transfer *via* the post-ligand exchange strategy remain to be fully understood. Nonetheless, these examples highlight the critical importance of thin shell thickness for achieving high CD and CPL activities. They also show the complexity of achieving such high-precision control in the synthesis of DRs when increasing their lengths and ARs. Obtaining DRs with both a high AR and a thin shell is a prerequisite for studying, controlling, and even increasing their ligand-induced CD and CPL activities.

Therefore in this work, we aimed to first analyse and understand the discrepancies in the literature concerning the temperature and time reaction conditions, then address the two issues mentioned above, and determine how thin the shell of a DR should be for optimal optical properties. To do so, we reinvestigated and modeled (1) the variation of the DRs' dimensions with time, (2) the effect of temperature throughout the synthesis on the DRs' shell thickness and (3) the effect of seed concentration on the aspect ratio of the thin-shell DRs. We eventually checked the influence of shell thickness on the chirality of asymmetric DRs.

2 Experimental section

2.1 Characterization

The TEM pictures were taken using an FEI Tecnai G2 F30 microscope (300 kV), Talos F200X G2 (200 kV) (Shenzhen), or a JEOL 2200 FS equipped with a field emission gun, operating at 200 kV and with a point resolution of 0.23 nm (Pessac). HRTEM micrographs were acquired with a GatanUltrascan CCD 2k-2k and digital diffractograms were calculated using the Gatan Digital Micrograph program. The UV/vis absorption measurements were performed using a TU-1901 double-beam UV/vis spectrophotometer (Beijing Purkinje General Instrument Co. Ltd, China), and the photoluminescence (PL) spectra were recorded on a fluoroSENS spectrophotometer (Gilden Photonics).

2.1.1 CD measurements. The measurements were conducted on Jasco J-815 and JASCO J-1500 CD spectrometers at a scan rate of 20 nm min^{–1}. All CD experiments were carried out in Milli-Q water with a quartz cuvette (0.1 cm path length, Hellma). In designing chiral nanoparticles for application, the



anisotropy or *g*-factor is a key parameter to determine optical activity as it can be easily determined by comparing the CD spectrum with the absorption spectrum. The equation is as follows: $g = \theta/3.298 \times 10^4 \times A$, where θ is the vertical coordinate of the CD spectrum, and A is the value in the absorption spectrum at the same concentration used to measure the CD spectrum.

All the heating mantles are made by Glas-Col but have different setups. (1) Typically, the experiments were performed by using a 180 W Series O spherical mantle (high capacity) covering both the top and the bottom of the flask to improve safety and efficiency; (2) we chose the 50% (90 W) input power controlled by the Glas-Col controller of lower power for control experiments, which decreases the heating rate (from ~ 12 K min $^{-1}$ to ~ 5 K min $^{-1}$).

2.2 Synthetic procedures

2.2.1 Chemicals. Tri-*n*-octyl phosphine oxide (TOPO, 99%), tri-*n*-octyl phosphine (TOP, 97%), tributyl phosphine (TBP, 97%), *n*-octadecyl phosphonic acid (ODPA, 97%), *n*-tetradecyl phosphonic acid (TDPA, 97%) and *n*-hexyl phosphonic acid (HPA, 97%) were purchased from Strem Chemicals. Cadmium oxide (CdO, 99.99%), sulfur (S, 99.98%), and selenium (Se, 99.99%) were purchased from Sigma-Aldrich. All chemicals were used as received without further purification.

2.2.2 Synthesis of the CdSe seeds. The synthetic procedure was based on the procedure reported in the literature. Typically, TOPO (1.5 g), ODPA (0.140 g), and CdO (0.030 g) were mixed in a 50 mL flask, heated to 423 K to form a colourless liquid (besides CdO), and alternately exposed to vacuum and argon at least 5 times. Then, to dissolve the CdO, the solution was heated to above 573 K under argon until it became optically clear and colourless, which indicated that the reaction between CdO and ODPA was complete. Then, the temperature was increased to 643 K, and 1.5 mL of TOP was injected into the flask, which caused the temperature to naturally decrease to 573 K. Then, a Se : TOP solution (0.4 mL, 1 mol L $^{-1}$) was injected at 653 K and reacted for several seconds. The size of the CdSe seed could be adjusted by altering the temperature, Cd : Se ratio, reaction time, and type of phosphonic acid (ODPA or TDPA).

Purification of the CdSe-TOP seed. The reaction mixture was cooled to 343–353 K and mixed with 50 μ L (40.85 mg) of TBP; then 4 mL of ethanol was added to the above solution, which was centrifuged at 10 000 rpm for 3 minutes. Then, the precipitate was dissolved in a small amount of toluene while the supernatant was discarded. After centrifugation again, the precipitate was dissolved in TOP (CdSe-TOP). Due to the TBP purification process, the CdSe seed can be better purified, removing the adsorbed ions on the surface and the by-products in the solution. This is essential for achieving uniform morphology control and high quantum yield in DRs.

2.2.3 Synthesis of the CdSe/CdS DRs. In a typical synthesis of CdSe/CdS nanorods *via* seeded growth, CdO (30 mg) was mixed in a 50 mL flask together with TOPO (1 g), ODPA (100 mg), and HPA (30 mg). After alternately exposing the flask to vacuum and argon at least 5 times at 423 K, the resulting

solution was heated to 573 K to make the solution completely transparent without any solids. Then, the temperature was increased to 593 K, and a mixed solution of S : TOP (0.5 mL, 2.5 mol L $^{-1}$) and the above CdSe-TOP solution (100 μ L) were injected into the flask. After injection, the temperature dropped to 543–573 K and then recovered to the pre-injection temperature within two minutes. The CdSe/CdS DRs were allowed to grow for approximately 8 minutes after the injection. Finally, the reaction mixture was cooled to room temperature, and the nanocrystals were separated from the side products and unreacted precursors using the same purification procedure as for the CdSe seed, except for the addition of TBP. After the reaction completion, a hair dryer was used to achieve rapid cooling and reduce the temperature by more than 100 K within the first minute, thereby effectively stopping the growth of CdSe/CdS DRs.

The shell thickness can be controlled by changing the injection temperature, heating mantle power, or ambient temperature. CdSe/CdS DRs with different aspect ratios were also synthesized by adjusting the seed concentration and reaction time.

3 Results and discussion

An analysis of the various syntheses proposed by various groups in the literature (Fig. 1 and Table 1) shows that the control of the shell thickness of these DRs is rather difficult and drastically depends on the temperatures and the working conditions. Based on these results, it was shown that temperature indeed played a major role at different stages of the synthesis, from room temperature to injection. Table 1 summarizes all the details, while Fig. 1 provides a quick overview of the detrimental effect of the temperature on the shell thickness. The control of the CdSe/CdS DRs' shell thickness is poor at such high injection temperatures, and the results may vary widely (Fig. 1 and Table 1) (as many as eight thicknesses could be obtained for one single temperature: 623 K).

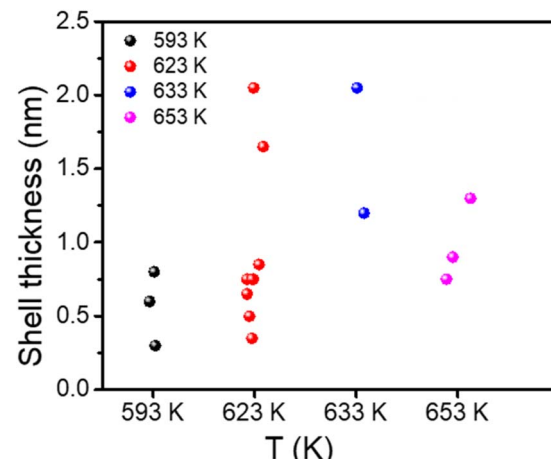


Fig. 1 Range of shell thicknesses of CdSe/CdS DRs for given temperatures and a reaction time of 8 min based on data from Table 1.



Table 1 List of various conditions used in the literature to synthesize CdSe/CdS DRs

No.	λ_{Abs} (nm)	Seed diam. (nm)	$T_{\text{injection}}$ (K)/time (min)	DR length (nm)	DR diam. (nm)	DR AR	Shell-thickness (nm)	Ref.
1	—	3.2	623	53 \pm 4	3.9 \pm 0.2	13.6	0.35	41
2		3.3	623	35 \pm 2	4.2 \pm 0.4	8.3	0.50	41
3		3.3	653	19 \pm 1	5.0 \pm 0.5	3.8	0.90	41
4	585	4.0 ^a	623/10	44 \pm 4	5.5 \pm 0.2	8.0	0.75	38
5	—	3.9 ^a	638	28 \pm 4	8 \pm 1	3.5	2.05	49
6		3.4 ^a	623	44 \pm 8	4.9 \pm 0.7	9.0	0.75	49
7		3.1 ^a	623	108 \pm 25	4.6 \pm 0.5	23.5	0.75	49
8	—	3.4 ^a	653	37 \pm 3	4.9 \pm 0.6	7.6	0.75	49
9		2.9 ^a	633	56 \pm 3	5.3 \pm 0.6	10.6	1.20	50
10	536	2.7	623/20	22	7	3.1	2.15	45
11			623	22	4	5.5	0.65	45
12			653/20	35	7	5.0	2.15	45
13			623/40	58	7	8.3	2.15	45
14	—	4.2	623	42	7.5	5.6	1.65	45
15	—	3.5	623/6	24.0 \pm 2	5.0 \pm 0.5	4.8	0.75	51
16	557	3.2 ^a	623	36.5	7.3	5.0	2.05	52
17	—	4.2	593	49 \pm 2.5	5.8 \pm 0.5	8.4	0.8	53
18			653 ^b	30.4 \pm 2.5	5.8 \pm 0.8	5.2	1.3	This work
19			623 ^b	32.5 \pm 2.0	4.9 \pm 0.5	6.6	0.85	This work
20			593 ^b	24.3 \pm 1.6	3.8 \pm 0.4	6.4	0.35	This work
21			593 ^c	24.5 \pm 2.0	4.4 \pm 0.5	5.6	0.6	This work

^a Diameter of the CdSe seed determined from the absorption spectrum using Peng's equation (nm);⁵⁴ ^b The ambient temperature was 303 K (summertime). ^c The ambient temperature was 291 K (wintertime); reaction time: 8 min, otherwise indicated.

To clarify the discrepancies between these results, we performed all the experiments with a temperature control located directly inside the solution to ensure more accurate monitoring of the reaction. Room-temperature solution injections were introduced into the solution only after it had reached and stabilized at the desired temperature.

We then decided to reinvestigate the growth of CdSe/CdS DRs by varying (i) the reaction time to follow the involved mechanisms, (ii) the reaction temperature to determine activation energies and optimize the AR range, and (iii) the concentration of CdSe seeds to offer even more versatility in the AR.

Typically, 3.2 nm wurtzite (WZ)-CdSe seeds⁵⁴ were chosen as starting seed samples ($\lambda_{\text{abs}} = 557$ nm, Fig. S1†) to study the growth process over a wide range of reaction times from 30 s to 16 min, with reaction temperatures extending from 503 to 653 K, and seed concentrations ranging from 4 to 40 μM .

3.1 Variation of the size of DRs with the reaction time

Peng *et al.*⁵⁵ investigated the growth of CdSe nanorods (NRs) and interpreted their data considering three main stages. (i) Initially, the 'spherical' CdSe nanocrystals grow isotropically; (ii) after a certain time, likely related to the development of well-defined facets, the so-called one-dimensional growth (1D) emerges when the axial growth rate is much higher than the almost negligible radial one; (iii) after another characteristic time, the NR growth becomes three-dimensional (3D), with growth occurring in both axial and radial directions. They mentioned that, during growth, NRs can also undergo some reshaping, which they attribute to the surface-to-bulk energy ratio that reduces the AR with little influence on the growth itself, as illustrated by the increase in NRs' volume.

Here we performed the first set of experiments starting from the same CdSe seed ($D_s = 3.2$ nm) at a concentration of 14 μM , and at 593 K. We varied the time and analysed the growth of the resulting CdSe/CdS DRs. Fig. 2 illustrates the precise control of their morphology, and Table 2 provides detailed information on the variation of the CdS shell thickness ($D - D_s/2$), the overall

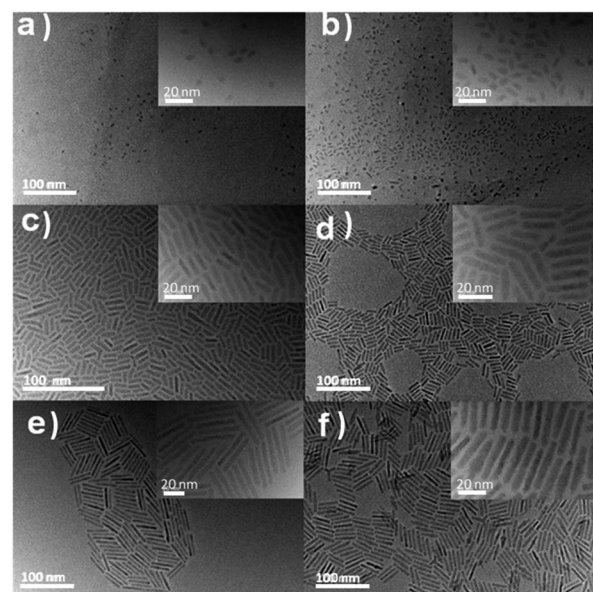


Fig. 2 TEM images of DRs (DR-1 to DR-6) synthesized under different reaction times starting with the same CdSe seed solution ($D_s = 3.2$ nm) at a concentration of 14 μM . (a) 30 s, (b) 60 s, (c) 120 s, (d) 240 s, (e) 480 s, and (f) 960 s.

length of the DRs (L), their overall aspect ratios ($AR = L/D$), and the increase in the overall volume with time.

As (i) the morphology of nanorods can be described as a cylindrical part with two hemispherical tips and (ii) cylinders and spheres have different symmetries, the growth law of the overall length L involves both axial and radial components. Then, we separate them considering that a NR, of overall length L and diameter D , can be described as a cylindrical part of length $l = L - D$ capped by two hemispherical tips of radius $D/2$. Fig. 3 shows a diagram of such a nanorod, depicting the growth sequence of the length (l), diameter (D), volume ($V - V_{\text{seed}}$) of the grown CdS material, and the aspect ratio, now defined as l/D ($l/D = L/D - 1$) to explicitly separate symmetries, for the seeded case where CdS grows over a CdSe seed at $T = 593$ K; raw data corresponding to this growth are provided in Table 2.

Schematically, the growth of DRs starting from the 3.2 nm seeds in the presence of ligands grafted on the surface shows the following stages, analogous to those observed by Peng under seedless conditions.⁵⁵ (i) When starting with polyhedron CdSe seeds of nearly spherical symmetry, the growth of a CdS layer on a seed remains isotropic until the emergence of facets that differentiate the surface energy properties (one CdS layer seems sufficient to induce such a differentiation). (ii) When this difference in surface energy becomes high enough,⁵⁶ the asymmetric growth is triggered along the axial direction. DRs form (1D-growth), and a maximum overall aspect ratio of 10 can be reached. (iii) Eventually, these DRs undergo 3D growth with some reshaping, likely to minimize surface energy stresses in comparison to bulk ones. This reshaping is evidenced by the concomitant decrease in length observed in Fig. 3b, and by the continuous volume growth with the reaction time, as shown in Fig. 3c.

The growth kinetic mechanisms of II-VI semiconductor DRs are not yet well established, particularly for the 1D-growth regime. On the one hand, Viswanatha *et al.*⁵⁷ investigated in detail the growth of bare CdS spherical nanoparticles during the Ostwald ripening regime and experimentally confirmed the validity of a diffusion-limited growth mechanism in this case. On the other hand, the growth mechanism of ligand-capped spherical CdSe nanoparticles remains a topic of debate. While half of the studies propose a diffusion-limited interpretation,^{58,59} the other half suggests a reaction-limited mechanism.^{60,61}

Nonetheless, when looking at the broader literature concerning the growth of metallic-capped nanoparticles, particularly gold ones⁶² (see also references therein), it looks like the growth of ligand-capped gold nanoparticles may follow different consecutive steps and mechanisms, but they are all driven by a surface reaction-limited process. Then, following these lines and considering the symmetry of the DRs, we examine the growth of the cylindrical part and the hemispherical tips separately.

For reaction-limited growth on CdSe seeds, well before the final Ostwald ripening, *i.e.*, in the free-growth regime during which the solute concentration at infinity ($[C]_{\infty}$) can be assumed constant, the growth of the DRs can be qualitatively obtained by balancing the DR volume growth rate with the reactive flux (J^{reac}) at the concerned surface of the DR.

Thus, axial growth occurs from the reaction flux at the spherical tips (index s) of the DRs such that we have $dV/dt|_D = V_M \cdot J_s^{\text{reac}} = V_M \cdot \pi D^2 k_s [C]_{\infty}$, whereas radial growth occurs from the reaction flux at the cylindrical part (index c) of the DRs so that $dV/dt|_l = V_M \cdot J_c^{\text{reac}} = V_M \cdot \pi D l k_c [C]_{\infty}$, where V_M is the molar volume of CdS and $k_{s,c}$ represents the reaction rates for solute incorporation into the DRs; $k_{s,c}$ is classically expressed in nm s^{-1} .⁶² Using the volume $V = \pi D^2 (l + 2D/3)/4$ of a DR, we, thus, expect the following growth rates (eqn (1)):

$$\left\{ \begin{array}{l} \frac{dl}{dt} \cong 4V_M k_s [C]_{\infty} \\ \frac{dD}{dt} \cong 2V_M \frac{l}{l+D} k_c [C]_{\infty} \end{array} \right. \quad (1)$$

In the 1D-growth regime, $l_{1d}(t) \cong 4V_M k_s [C]_{\infty} t$ and $dD_{1d}/dt \approx 0$, so that $D_{1d}(t) = D_{1d}^0$, where D_{1d}^0 is the size of the spherical CdS-covered CdSe seeds at the beginning; in our case D_{1d}^0 should correspond to D_s , the size of the spherical seeds covered with one CdS layer, as illustrated in Fig. 3b. Therefore, in this 1D-growth regime, we expect the length, l , to behave linearly over time and the diameter, D , to remain almost constant with a size close to the seed size. This is what we observe experimentally in Fig. 3b; this is further confirmed by a power-law fit of the length dynamics which gives an exponent of 1.007 with a correlation close to 0.99.

Moreover, in this 1D-growth regime, the volume of the DRs corrected by the volume of the seed ($V_{1d} - V_{\text{seed}}$), *i.e.*, the amount of grown material, and the aspect ratio, $AR_{1d} = l_{1d}/D_{1d}$,

Table 2 Variation of the physical characteristics of CdSe/CdS DRs with the reaction time (CdSe seed diameter $D_s = 3.2$ nm and a concentration of 14 μM) at 593 K

Name	React time (s)	Length L (nm)	D (nm)	AR L/D	Shell-thickn. $(D - D_s)/2$ (nm)	V^a (nm^3)
DR-1	30	5.5 ± 0.9	3.4 ± 0.5	1.6	0.1	39.6
DR-2	60	8.0 ± 1.0	3.6 ± 0.5	2.2	0.2	69.2
DR-3	120	15.7 ± 3.0	3.6 ± 0.4	4.4	0.2	147.6
DR-4	240	21.7 ± 2.7	3.8 ± 0.4	5.7	0.3	223.8
DR-5	480	38.7 ± 3.5	3.6 ± 0.4	10.8	0.35	381.4
DR-6	960	35.8 ± 2.4	5.4 ± 0.8	6.6	1.1	778.7

^a Overall volume $V = \pi D^2 (l - D/3)/4$, assuming a cylindrical part with hemispherical ends.



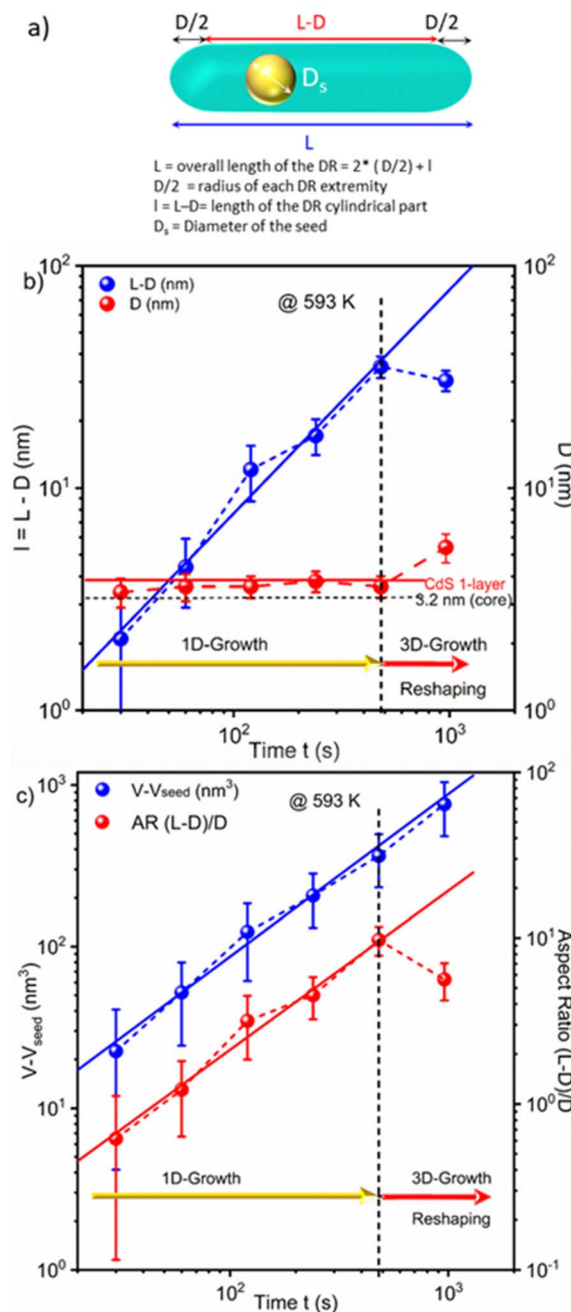


Fig. 3 (a) Schematic of a DR (dot in a rod) with all the distances used in the manuscript. (b) Linear variation of the length ($l = L - D$) on the cylindrical part with time. Note that the diameter D remains constant (1D-growth); 3D growth and/or reshaping occurs after a reaction time onset of around 8 minutes under the present experimental conditions. (c) Linear variation of the CdS DR volume ($V - V_{\text{seed}}$) and the cylindrical-to-spherical aspect ratio (l/D) with time; the persistence of the linear variation of the volume of CdS beyond 8 minutes (480 s: vertical dotted line) suggests a DR reshaping. CdSe seed (3.2 nm) at a concentration of 14 μM and $T = 593$ K; see text for the data fitting.

are also expected to behave respectively as $(V_{1d} - V_{\text{seed}})(t) \approx \pi l_{1d}(t)D_{1d}^{0.2}/4 = \pi D_{1d}^{0.2}V_M k_s [C]_\infty t$ and $\text{AR}_{1d}(t) = l_{1d}(t)/D_{1d}^0 \approx 4V_M k_s [C]_\infty t/D_s$, both linearly varying with time. This is experimentally determined and again confidently fitted using power-

laws with respective exponents of 1.006 and 0.96 and correlations of 0.99 and 0.98. Note also that a linear fit of $(V_{1d} - V_{\text{seed}}) \approx \pi l_{1d}(t)D_{1d}^{0.2}/4$ as a function of l_{1d} before reshaping, gives a slope of $\pi D_{1d}^{0.2}/4 = (12.14 \pm 0.22)$ nm², from which we can deduce a statistical average diameter of $D_{1d}^0 = (3.93 \pm 0.04)$ nm during the 1D-growth phase. This value corresponds to the seed diameter, $D_s = 3.2$ nm covered with a single CdS layer (≈ 0.35 nm) and, thus, strongly supports the fact that the first transitory isotropic growth stage of CdS onto the spherical CdSe seeds involves the growth of just a monolayer of CdS to trigger the 1D-growth. We finally note that DRs eventually reshape when their overall aspect ratio reaches a maximum value of $(l_{1d}/D_{1d} + 1) \approx 11$ under the present experimental conditions. However, this reshaping does not affect the growth as illustrated by the continued linear variation of the DR volume with time, despite the decrease in their length.

This dynamic thus suggests a method to consistently produce high aspect ratio NRs with the thin-shell thickness remaining around 1 CdS monolayer as long as the growth remains within the 1D-regime, *i.e.*, up to a reaction time of 8 minutes under the present experimental conditions. Indeed, for longer reaction times, the 3D growth and reshaping increase the shell thickness and decrease the AR, explaining why many previous studies used these 6–10 min reaction times.^{38,41,45,49–51,63} Considering the data in Fig. 3, we also chose 8 min as the reaction time and further optimized the control over the AR by varying the reaction temperature.

The shape and composition of samples were confirmed by TEM energy dispersive spectroscopy (EDS) elemental mapping and shown for one of them (Fig. 4). The position of the CdSe seed at around 1/4 to 1/2 of the overall length shows that the temporal sequence of the seeded rod length is consistent with the literature.^{40,49,64–67}

3.2 Variation of the shell thickness of the DRs with reaction temperature

To clarify the discrepancies observed in Fig. 1 over the 593–653 K temperature range, Fig. 5, S2[†] and Table 3; illustrate and detail the variation in the DRs' length and CdS shell thickness when controlling the temperature inside the reactor and varying this temperature over a wide range (503–653 K), including those in Fig. 1.

Fig. 5 shows that 1D-growth is preserved for at least 8 min, provided the injection temperature remains below 593 K. The shell thickness can, thus, remain very thin while the overall length L of the DRs, and consequently the overall aspect ratio L/D , can be tuned up to 6.4 under present experimental conditions.

Moreover, using the data from Table 3, and the linearity between $(V_{1d} - V_{\text{seed}})$ and l_{1d} in the 1D-growth regime ($(V_{1d} - V_{\text{seed}})(t) \approx \pi l_{1d}(t)D_{1d}^{0.2}/4$), we find $\pi D_{1d}^{0.2}/4 = (12.07 \pm 0.20)$ nm² from which we can deduce a statistical average final diameter of $D_{1d}^0 = (3.92 \pm 0.03)$ nm. This value, now obtained from experiments conducted at different temperatures after an 8-minute reaction time, strengthens the fact that just a single CdS monolayer (0.35 nm) grows on the CdSe seeds ($D_s = 3.2$ nm)

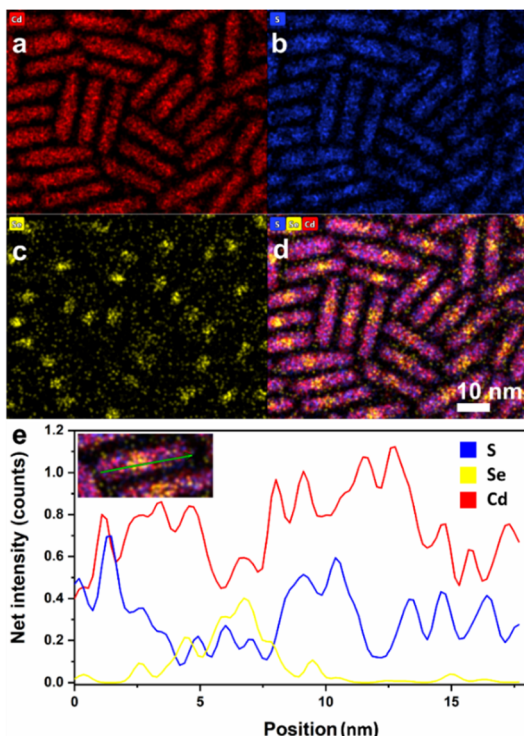


Fig. 4 Representative TEM EDS mapping of one of the many samples, DR15, with a length of 18.3 ± 2.8 nm and a diameter of 3.8 ± 0.6 : (a–c) representative EDS mapping images for Cd, S, and Se, (d) merging of Cd, S, and Se maps, and (e) line-scan distribution profiles of Cd, S, and Se in a DR.

during the first growth stage, regardless of the reaction temperature.

Also, temperature investigations give access to activation energies necessary for DR growth. On the one hand, let $\tau_{1,3}$ denote the crossover time at which the growth switches from 1D to 3D. Then, the axial growth rate $dl/dt \equiv 4V_M k_s [C]_\infty$ continues to predict $l_{3d}(t) \equiv 4V_M k_s [C]_\infty t$. Moreover, as $l/D \gg 1$ at $\tau_{1,3}$ in Fig. 5, the radial growth rate $dD/dt \approx 2V_M l/l + Dk_c [C]_\infty \approx 2V_M k_c [C]_\infty$ leads to $D_{3d}(t) \approx D_{1d}^0 + 2V_M k_c [C]_\infty (t - \tau_{1,3})$. We deduce the CdS shell thickness variation, $S_{3d}(t > \tau_{1,3}) = (D_{3d} - D_{1d}^0)/2 \approx V_M k_c [C]_\infty (t - \tau_{1,3})$. On the other hand, the DR growth reaction rate constants, $k_{s,c}$, of the solute are known to follow Arrhenius' laws in temperature of the form $k_{s,c} = k_{s,c}^0 \exp(-E_{s,c}/RT)$, where $E_{s,c}$ represents the growth activation energies at the DR surfaces, at their spherical tips and the cylindrical part, respectively. Consequently, at a given time and for an initial solute concentration of $[C]_\infty$, we expect: (i) $l_{1d,3d}(T) \propto k_s(T) \propto \exp(-E_s/RT)$ during the 1D- and the 3D-growth stages and, (ii) $S_{3d}(T) \propto k_c(T) \propto \exp(-E_c/RT)$ for the 3D-growth stage. Thus, the temperature-dependent variations in the DR shell thickness and length should allow the determination of the corresponding axial and radial energies of activation (Fig. 5).

The axial growth exponential fitting yields $E_s \approx (51 \pm 8)$ kJ mole $^{-1}$. The determination of E_c from the 3D-radial growth stage is less accurate because it is difficult to obtain much data free from DR reshaping; only an order of magnitude can be

given using three shell thickness measurements. The corresponding exponential fitting yields $E_c \approx (70 \pm 18)$ kJ mole $^{-1}$. Considering the errors resulting from data fitting, $E_c \sim E_s$, which suggests that the energy cost for radial and axial solute incorporation is not a determinant quantity to explain the difference between 1D- and 3D-growth.

Activation energy data are scarce in the literature for comparison. For instance, Viswanatha *et al.*⁵⁷ performed experiments on the growth of CdS nanoparticles in the absence of surface ligands and over a narrow and low-temperature range (333–373 K); they also adjusted their concentrations to maintain the growth of their CdS nanoparticles in the spherically isotropic Ostwald ripening regime. They found an activation energy of $E_a \sim 142 \pm 3$ kJ mole $^{-1}$, *i.e.*, typically twice as high as the E_s obtained for the 3D-growth at the DR tip with the same spherical symmetry. Nonetheless, both the presence of ligands on the DR surface, which are known to reduce diffusion phenomena, and the higher reaction temperature (503–653 K) level may explain this difference in values. This hypothesis is strengthened by another work on the spherical growth of CdS nanocrystals in a hot paraffin matrix developed by Yordanov *et al.*⁶⁸ Working in the spherically isotropic Ostwald ripening regime, they found that the growth rate was slower when using a coordinating matrix (Tri-*n*-octyl phosphine oxide, (TOPO)) instead of a non-coordinating one (tributylphosphine sulfide (TBP-S) in liquid paraffin). Further analysis using TBP-S gave an activation energy of $E_a \sim 51.9$ kJ mole $^{-1}$ within the temperature range of 473–533 K,⁶⁹ comparable to our measured value (average value: $E_s \sim 60$ kJ mole $^{-1}$).

Consequently, the reaction temperature plays a crucial role in the growth process, and 593 K seems to be an optimized value

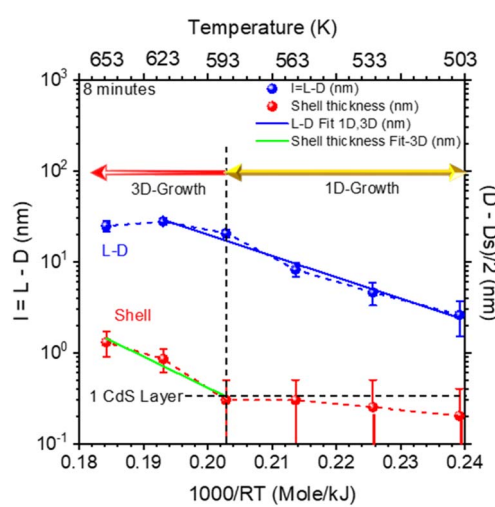


Fig. 5 Variation of the cylindrical length, $l = L - D$, and the shell thickness, $S = (D - D_s)/2$, with the injected thermal energy after an 8-minute reaction time; the corresponding injection temperatures are indicated on the top axis. During the 8-min reaction time, the 1D-growth regime is preserved up to 593 K. Beyond this temperature, the growth shifts toward the 3D-growth regime; eventually, DR reshaping also occurs within the 8-min reaction time necessary for the reaction temperature to reach 623 K. CdSe seeds (3.2 nm) at a concentration of $18.8 \mu\text{M}$ and $T = 593$ K; see text for the data fitting.



Table 3 The physical characterization of CdSe/CdS DRs obtained at different injection temperatures in the same CdSe seed solution ($D_s = 3.2$ nm). [CdSe] = 18.8 μM with a shell growth time of 8 min

Name	$T_{\text{Injection}}$ (K)	Length L (nm)	Diameter D (nm)	AR l/D	$(D - D_s)/2$ (nm)	Volume ^a V (nm^3)
DR-7	503	6.2 ± 0.7	3.6 ± 0.4	1.7	0.2	50.9
DR-8	533	8.3 ± 0.8	3.7 ± 0.5	2.2	0.25	76.0
DR-9	563	12.0 ± 1.0	3.8 ± 0.4	3.2	0.3	121.7
DR-10	593	24.3 ± 1.6	3.8 ± 0.4	6.4	0.3	261.2
DR-11	623	32.5 ± 2.0	4.9 ± 0.5	6.6	0.85	582.1
DR-12	653	30.4 ± 2.5	5.8 ± 0.8	5.2	1.3	752.1

^a Overall volume $V = \pi D^2(L - D/3)/4$, assuming a cylindrical shape with two hemispherical ends.

for achieving the highest aspect ratio before 3D growth and reshaping occur. Finally, this temperature-controlled investigation clarifies the dispersion in results observed in previous studies, many of which were based on reaction temperatures above 623 K.^{38,41,45,49–51,63}

3.3 Variation of the thin-shell DR aspect ratio with the seed concentration

DRs with different aspect ratios have mostly been obtained in the literature by varying the seed diameter,^{41,48,50,70} reaction time,^{40,45} ligands,³⁴ or amounts of precursors.^{16,71–73} We propose an additional parameter in the present work: the concentration [CdSe] of the CdSe seeds in solution (Fig. 6, 7 and Table 4).^{20,34}

Table 4 shows that the shell-thickness of the DRs remains less than 1 monolayer (one monolayer of CdS having an average thickness of 0.35 nm) as the seed concentration decreases. Meanwhile, their length not only increases (Fig. 6) but also exhibits a much narrower size distribution.

These behaviors can be quantitatively understood by mass conservation at time t . Indeed, the volume of material consumed at time t for DR growth, $V_M[C(t)] = V_M \times \text{Min}\{[\text{Cd}](t), [\text{S}](t)\}$, should be equal to the number of seeds per liter, N_s , multiplied by the increase in individual DR volume due to material consumption: $N_s(V(t) - V_{\text{seed}})$. Then, as $N_s = \mathcal{N}[\text{CdSe}]$, where \mathcal{N} is the Avogadro number, we deduce (eqn (2)):

$$(V(t) - V_{\text{seed}}) \cdot \mathcal{N}[\text{CdSe}] = V_M[C(t)] \quad (2)$$

Working in the 1D-growth regime, $(V(t) - V_{\text{seed}}) \approx (V_{1d} - V_{\text{seed}})(t) \approx \pi l_{1d}(t)(D_{1d}^0)^2/4$, where $D_{1d}^0 = D_s + 2\text{CdS}$ layers ($D_s = 3.2$ nm plus twice 0.35 nm). Then, at a given reaction time (8 min), temperature (593 K) and cadmium precursor concentration ($[\text{Cd}] = 0.55$ M), we expect from eqn (2): $l_{1d} \propto (V_{1d} - V_{\text{seed}}) \propto [\text{CdSe}]^{-1}$, $D_{1d} = D_{1d}^0 \propto [\text{CdSe}]^0$, and $\text{AR}_{1d} = \frac{l_{1d}}{D_{1d}} \approx \frac{l_{1d}}{D_{1d}^0} \propto [\text{CdSe}]^{-1}$, all linear in $[\text{CdSe}]^{-1}$, except $D_{1d} \sim D_s$ which is fixed as the initial condition.

Moreover, the diameter D of the DRs remains constant over the investigated range of CdSe seed concentrations, corresponding to almost one order of magnitude variation. Finally, Fig. 7 shows that $(V_{1d} - V_{\text{seed}})$ is indeed linear in l_{1d} , and the slope of $\pi D_{1d}^0/4 = (10.75 \pm 0.21) \text{ nm}^2$, allows deducing a statistical mean diameter of $D_{1d}^0 = (3.70 \pm 0.04) \text{ nm}$, during 1D-

growth. This value corresponds to a seed diameter of $D_s = 3.2$ nm covered with a single CdS layer (0.35 nm) and gives one more proof of the isotropic growth of a single CdS shell before switching to the 1D-growth regime.

In conclusion, CdSe/CdS DRs with a thin shell close to a single CdS layer can be synthesized with high accuracy and predictability when the reaction temperature is well controlled, including the influence of the initial thermal conditions (see the ESI (Tables S1 and S2)).[†] This approach was also extended to other CdSe seed sizes (Fig. S3 and S4 and Table S3[†]). Moreover, their overall aspect ratio can be continuously varied between 1 and 20 (DR13), just by adjusting the reaction time and/or seed concentration at the optimized reaction temperature. Finally, as illustrated in Fig. 3 over time and Fig. 5 with varying temperatures, the 3D-growth process enables variations and adjustments in the shell thickness as needed. Consequently, we had a set of available samples for studying in detail the influence of the envelope and length on the chiroptical properties of these CdSe/CdS nano-objects.

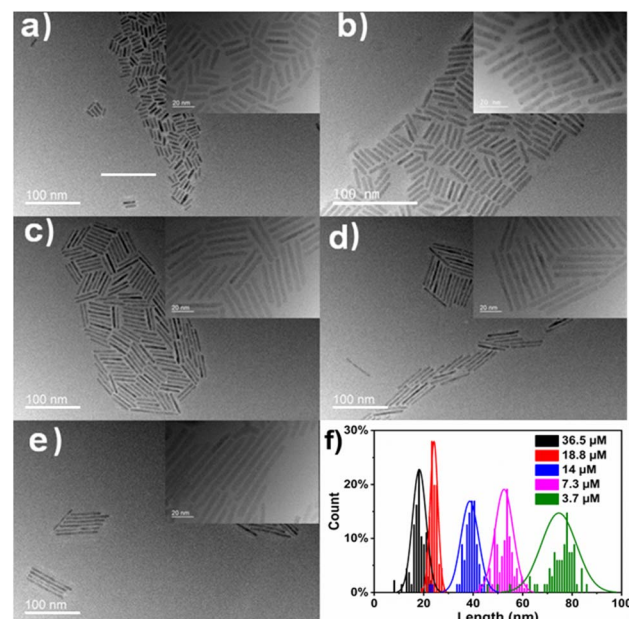


Fig. 6 TEM images of DRs synthesized starting with different CdSe seed concentrations. (a) DR-15, 36.5 μM , (b) DR-10, 18.8 μM , (c) DR-5, 14 μM , (d) DR-14, 7.3 μM , and (e) DR-13, 3.7 μM , and (f) variation of DR length distributions obtained at different seed concentrations (593 K).



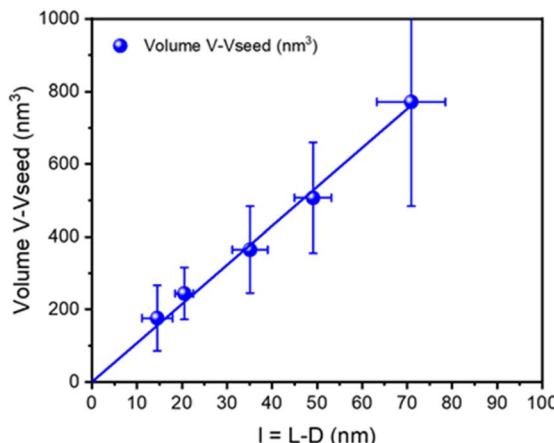


Fig. 7 Linear variation of the volume $V - V_{seed}$ of the DRs versus the length $l = L - D$ of their cylindrical part in the 1D-growth regime, at $T = 593$ K and after 8 min of reaction, when varying the seed concentration $[CdSe]$.

3.4. Influence of the shell thickness on the chirality of DRs

To check how the shell thickness can affect the CD g -factor signal of chiral DRs, we selected a series of DRs with four different shell thicknesses ranging from 0.35 to 2.0 nm (DR-10, DR-11, DR-12, and DR-23 (Table S4†), ARs ranging from 3.5 to 6.6, and lengths about 25–30 nm. The thickest shell (DR-23) was obtained with a method combining an established fast-injection-based step for Cd and S precursors to create the initial shell, followed by a second slow injection growth that allows for systematic variation of the shell thickness while maintaining a high degree of monodispersity at the batch level and uniformity at the single-nanorod level, as reported by Bawendi's group.³⁸ The shell thickness increased to 2.0 nm through two slow-growth steps separated by a purification step (Fig. S5†). The UV-vis and PL spectra of the samples are shown in Fig. S6 and S7.†

We chose ligand-induced chirality among the several methods for inducing chirality in QDs.^{2,3,16,20} Induced chirality in the aqueous phase relies on the replacement of the original achiral ligand with a chiral one on the semiconductor nanoparticles.^{15,16,29,30,74} Gun'ko and co-workers were the first to report the observation of circular dichroism (CD) response induced in excitonic transitions of CdS quantum dots (QDs)

capped with chiral molecules.¹⁸ However, the CD g -factor they found was quite low (typically 10^{-4} or even 10^{-5}).^{16,75–78} Since, on the one hand, the induced chiral signal intensity of the core-shell systems has been shown to increase with decreasing shell thickness,²⁴ and on the other hand, we have recently observed that CdSe/CdS DRs have great potential for high ligand-induced chirality,^{16,17} we aim to use our actual control of shell thickness down to ultra-thin shell DRs to generate and study high ligand-induced chiral signals.

To prepare these chiral DRs, we extracted the organic colloidal phase using an aqueous phase with cysteine (Cys) ligands as previously discussed (Fig. 8).^{16,17}

To do so, cysteine was dissolved in deionized (DI) water (5 mL, $[Cys] = 0.1$ M); the pH of the resulting solution was then adjusted to 12.0 with a 25% aqueous solution of tetramethyl-lammonium pentahydrate (TMAH). A solution of CdSe/CdS DRs in *n*-hexane (5 mL, 1 μ M) was added to the aqueous cysteine solution; the reaction mixture was then purged with nitrogen and stirred at room temperature, under an inert atmosphere for 24 h in the absence of light. The reaction mixture was then allowed to rest for 1 h to allow phase separation. The bottom aqueous layer, now containing the DRs, was removed with a syringe, and purified twice by precipitation with ethanol/DI water/chloroform (4 : 1 : 1). As an example, purified Cys-DRs were dispersed in deionized H_2O and stored at room temperature in the dark. Fig. S8† shows the luminescence of the DRs listed in Table 3; before (a and b) and after (c and d) the ligand exchange and transfer from the organic to the aqueous phase. From left to right, we observe the CdSe QDs, and DRs with different aspect ratios, respectively. The luminescence of the different DRs is well preserved, but that of the pure CdSe is almost completely quenched.

We then focused on the UV-vis and CD studies performed on samples with increasing shell thicknesses with also comparable lengths, listed in pairs in Table S4† and shown in Fig. 9.

The results show that the strong CD signal observed for CdSe/CdS DRs with one or two monolayers (DR-10 and DR-11) decreases and is completely suppressed when the shell becomes thicker (DR-12 and DR-23), as expected due to the effect mediated by hole interactions with the surface. This phenomenon is independent of the DR length, as illustrated by the similar lengths of DR-10 and DR-23. The CD g -factor signal decreased by more than 5-fold as the shell thickness increased

Table 4 Physical characterisation of CdSe/CdS DRs prepared using increasing seed concentrations of the same CdSe seeds ($D_s = 3.2$ nm); $T = 593$ K, $[CdO] = 0.55$ M

Name	[Seed] ^a (μ M)	Length (nm)	Diam. (nm)	AR ^b	Shell-thickness (nm)	V^c (nm^3)
DR-13	3.7	74.6 ± 7.1	3.7 ± 0.5	20.2 (19.2)	0.3	788.84
DR-14	7.3	52.7 ± 3.7	3.6 ± 0.4	14.6 (13.6)	0.2	524.21
DR-5	14	38.7 ± 3.5	3.6 ± 0.4	10.8 (9.8)	0.2	381.7
DR-10	18.8	24.3 ± 1.6	3.8 ± 0.4	6.4 (5.4)	0.3	261.24
DR-15	36.5	18.3 ± 2.8	3.8 ± 0.6	4.8 (3.8)	0.3	193.17

^a The seed concentration was calculated from the absorption spectrum using Peng's equation (nm).⁵⁴ ^b AR = L/D ($(L - D)/D$). ^c Overall volume $V = \pi D^2(L - D/3)/4$, assuming a cylindrical shape with hemispherical ends.



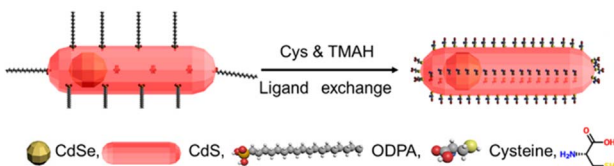


Fig. 8 The ligand exchange process of DRs from the oil phase to the aqueous phase.

from 0.35 to 2.10 nm (one to six layers) (Fig. 10, Tables S5 and S6†), as also observed by Purcell-Milton.²⁴

This study not only confirms, the behaviour observed by Purcell *et al.*^{24,79} in QDs for DRs, *i.e.*, an inverse relationship between the CD g-factor and the number of shell layers (consistent with the increase in the distance between the chiral ligands and the holes localized at the CdSe core level) but also shows that this behaviour (i) takes place in a range of g-values an order of magnitude higher than in QDs, (ii) is linear, and (iii) does not follow an exponential trend.

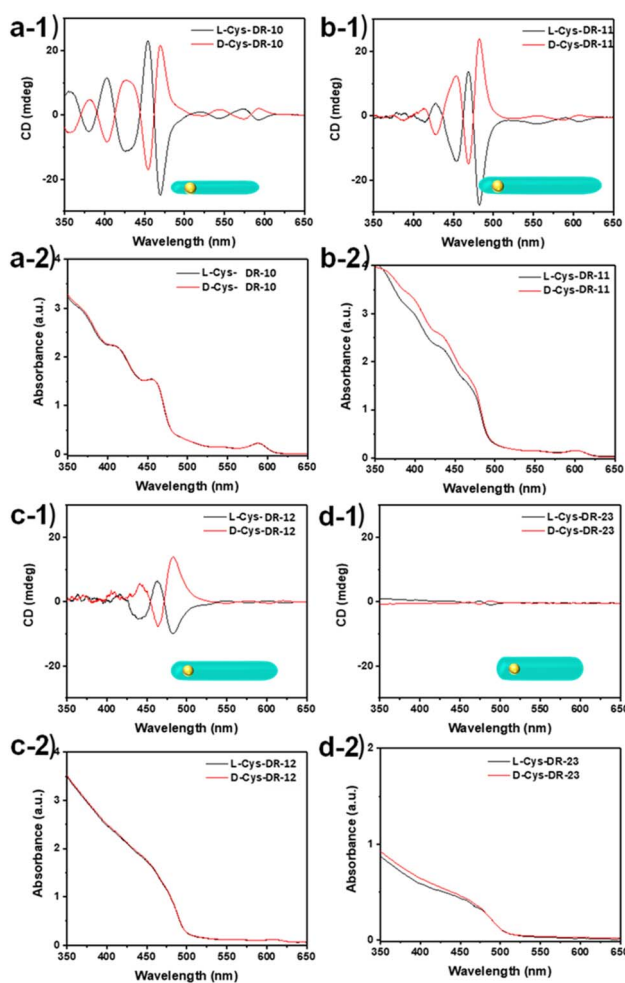


Fig. 9 CD spectra and the corresponding UV/vis absorption spectra of the L- and D-Cys-CdSe/CdS DRs with different shell thicknesses. (a) DR-10, (b) DR-11, (c) DR-12, and (d) DR-23.

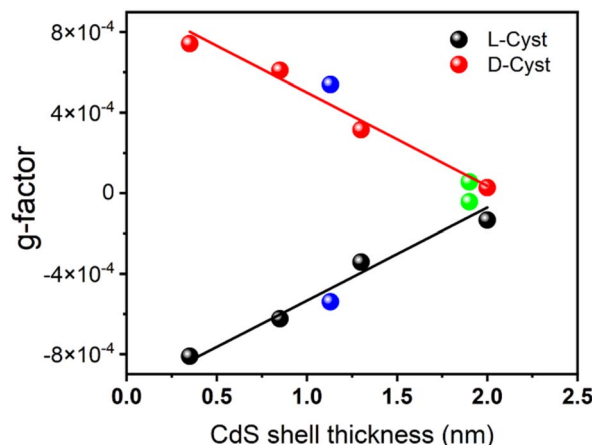


Fig. 10 Variation of the CD g-factor of the DRs with their shell thickness (Table S4†). Green dots: additional data from ref. 16 (Tables S2 and S3†) and blue ones from ref. 34 with identical seed diameter.

3.5 Influence of the length of the DRs on their chirality

We also demonstrated that the main consequence, *i.e.*, the decrease in coupling between the seed holes and the chiral source, also depends on the DR length. Indeed, as illustrated in Fig. 11a–e, the symmetrical CD signal intensities of both L- and D-modified surfaces measured at the maximum wavelength (~475 nm) increase with the aspect ratio of the nanorods (see Table 3 (AR), S7, and S8† (CD anisotropy g CD-factors)), with values ranging from 0.23×10^{-3} to 1.3×10^{-3} when varying the

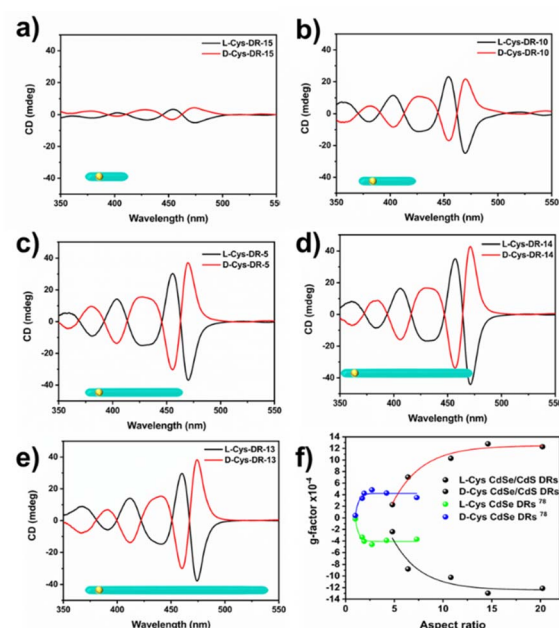


Fig. 11 Variation of the CD signal with the DR aspect ratio, in the 400–500 nm region of the CdS absorption (CdSe seed size $D_s = 3.2$ nm). (a–e) CD signal of DR-15, DR-10, DR-5, DR-14, and DR-13, from Table 3; (f) Resulting CD g-factor variation of the same DRs (lines are guides for the eyes). Blue and green data are from ref. 78 for pure CdSe QRs. Lines are also guides for the eyes.



AR from 4.8 to 14.6. It then remained constant at more than 10^{-3} as the AR continued to increase (Fig. 11f). To the best of our knowledge, this is the first report on CdSe/CdS DRs with such high-induced chirality (more than 10^{-3}) using a single small molecule. Although Kuang *et al.*³⁴ reported CD g-factors of 1.2×10^{-3} , they used a mixture of two different ligands (D-cysteine and D-histidine), whereas each ligand, on its own, induced a CD g-factor of only 0.52×10^{-3} .

A closer look at Fig. 11 further highlights the significant added value of a thin CdS shell as compared to pure CdSe nanorods.⁷⁸ The combined effects of the CdSe core and CdS shell generate a chiral signal for the CdSe/CdS DRs that is higher than that of pure CdSe or CdS. As the aspect ratio increases, the CdS shell gradually grows along the [001] axis, which increases the anisotropy and leads to chirality enhancement.

4 Conclusions

In this work, we have shown that DR synthesis is finely driven by a temperature-dependent two-step mechanism. Using CdSe seeds with a regular polyhedral morphology, the first transient stage involves growing a very thin, wurtzite-CdS⁶⁴ spherical shell with a thickness close to one atomic layer. The second stage is triggered by the emergence of facets with different surface energies on this CdS layer that drive the growth to become anisotropic and promote the DR morphology (so-called 1D-growth by Peng⁵⁵). The increase in the AR, while maintaining a thin shell, has been optimized by fine-tuning (i) the reaction time (which must be around 8 min), (ii) the reaction temperature (injection and ambient temperature and power of the heating mantle) (which must be around 593 K), and (iii) the seed concentration (close to 10 μM for AR > 10). Playing with all these parameters, we successfully prepared DRs with an ultra-thin shell layer and different ARs up to 20 (Table 3).

The reaction temperature plays a crucial role in the growth process, and 593 K appears to be the optimized value for which the highest AR is reached before 3D growth and reshaping take place. Eventually, this study on the control of the temperature elucidates the discrepancies in results observed in the aforementioned studies, where many used reaction temperatures above 623 K.

Under optimal conditions, we could achieve DRs with a thin shell thickness of approximately 0.35 nm, corresponding to a single atomic layer of CdS and ARs ranging from 4.8 to 20. Their CD g-factor values varied from 0.23×10^{-3} to 1.30×10^{-3} . Notably, the CD g-factor value of 1.3×10^{-3} represents the highest ligand-induced chirality achieved to date for this type of nanorods by simply controlling their length and shell thickness. Additionally, only one type of chiral ligand was used. This approach gives these structures great potential for further applications in the chirality domain. Most of all, this study provides a platform for the exploration of various dimensions of nanostructures with controllable anisotropy. Finally, we anticipate that this ultra-thin shell adjustment strategy can be extended to other types of seed-grown semiconductor

nanoparticles, enhancing their chiral signal and catalytic properties with significant practical implications.

Data availability

The authors confirm that the data supporting the findings of this study are available within the article [and/or its ESI†].

Author contributions

The manuscript was written through the contributions of all authors. All authors have approved the final version of the manuscript.

Conflicts of interest

There are no conflicts to declare.

Acknowledgements

TEM data were obtained using microscopes at the Plateforme Aquitaine de Caractérisation des Matériaux (PLACAMAT, UMS 3626, CNRS, Univ. Of Bordeaux, Pessac, France) and the Southern University of Science and Technology Core Research Facilities. The authors acknowledge the technical support from Marion Gayot at PLACAMAT, as well as Dongsheng He and Yang Qiu at SUSTech CRF (Nouveaux Matériaux 2020 and 2021). The authors acknowledge the funding support from the National Key Research and Development Program of China (No. 2022YFB3602903, 2021YFB3602703, and 2022YFB3606504), the National Natural Science Foundation of China (No. 62204107 and 12204318), the Guangdong Basic and Applied Basic Research Foundation (No. 2022A1515011614 and 2021A1515110535), the Shenzhen Science and Techn. Program (No. JCYJ20220818100411025 and RCYX20221008092908030), the Shenzhen Key Laboratory for Advanced Quantum Dot Displays and Lighting (No. ZDSYS201707281632549), the Pingshan District Innovation Platform Project of Shenzhen Hi-tech Zone Development Special Plan in 2022 (29853M-KCJ-2023-002-01), and the Natural Science Foundation of Top Talent of SZTU (grant no. GDRC202344 and GDRC202340). P. M.-B acknowledges funding from the Deutsche Forschungsgemeinschaft (DFG, German Research Foundation) under Germany's Excellence Strategy – EXC 2089/1 – 390776260. P. L. and W. C. gratefully acknowledge financial support from the Chinese Scholarship Council (CSC). MHD and JPD acknowledge the CNRS through the MITI interdisciplinary programs (Action MITI: Nouveaux Matériaux 2020 and 2021).

Notes and references

- 1 A. Ben-Moshe, A. O. Govorov and G. Markovich, *Angew. Chem., Int. Ed.*, 2013, **52**, 1275–1279.
- 2 J. Yeom, B. Yeom, H. Chan, K. W. Smith, S. Dominguez-Medina, J. H. Bahng, G. Zhao, W.-S. Chang, S.-J. Chang, A. Chuvilin, D. Melnikau, A. L. Rogach, P. Zhang, S. Link, P. Král and N. A. Kotov, *Nat. Mater.*, 2014, **14**, 66.



3 M. V. Mukhina, V. G. Maslov, A. V. Baranov, A. V. Fedorov, A. O. Orlova, F. Purcell-Milton, J. Govan and Y. K. Gun'ko, *Nano Lett.*, 2015, **15**, 2844–2851.

4 A. Kühnle, T. R. Linderoth, B. Hammer and F. Besenbacher, *Nature*, 2002, **415**, 891–893.

5 A. Ben-Moshe, A. Teitelboim, D. Oron and G. Markovich, *Nano Lett.*, 2016, **16**, 7467–7473.

6 G. Yang and H. Zhong, *Isr. J. Chem.*, 2019, **59**, 639–648.

7 S. Huo, P. Duan, T. Jiao, Q. Peng and M. Liu, *Angew. Chem., Int. Ed.*, 2017, **56**, 12174–12178.

8 Y. Xia, Y. Zhou and Z. Tang, *Nanoscale*, 2011, **3**, 1374–1382.

9 M. Sun, L. Xu, A. Qu, P. Zhao, T. Hao, W. Ma, C. Hao, X. Wen, F. M. Colombari, A. F. de Moura, N. A. Kotov, C. Xu and H. Kuang, *Nat. Chem.*, 2018, **10**, 821–830.

10 E. Shah and H. P. Soni, *RSC Adv.*, 2013, **3**, 17453–17461.

11 L. Xiao, T. An, L. Wang, X. Xu and H. Sun, *Nano Today*, 2020, **30**, 100824.

12 W. Ma, L. Xu, A. F. de Moura, X. Wu, H. Kuang, C. Xu and N. A. Kotov, *Chem. Rev.*, 2017, **117**, 8041–8093.

13 X. Zhao, S.-Q. Zang and X. Chen, *Chem. Soc. Rev.*, 2020, **49**, 2481–2503.

14 X. Liu and R.-H. Jin, *Chem. Synth.*, 2022, **2**, 7.

15 U. Tohgha, K. K. Deol, A. G. Porter, S. G. Bartko, J. K. Choi, B. M. Leonard, K. Varga, J. Kubelka, G. Muller and M. Balaz, *ACS Nano*, 2013, **7**, 11094–11102.

16 J. Cheng, J. Hao, H. Liu, J. Li, J. Li, X. Zhu, X. Lin, K. Wang and T. He, *ACS Nano*, 2018, **12**, 5341–5350.

17 J. Hao, Y. Li, J. Miao, R. Liu, J. Li, H. Liu, Q. Wang, H. Liu, M.-H. Delville, T. He, K. Wang, X. Zhu and J. Cheng, *ACS Nano*, 2020, **14**, 10346–10358.

18 M. P. Moloney, Y. K. Gun'ko and J. M. Kelly, *Chem. Commun.*, 2007, **38**, 3900–3902.

19 S. D. Elliott, M. P. Moloney and Y. K. Gun'ko, *Nano Lett.*, 2008, **8**, 2452–2457.

20 Y. Zhou, M. Yang, K. Sun, Z. Tang and N. A. Kotov, *J. Am. Chem. Soc.*, 2010, **132**, 6006–6013.

21 T. Nakashima, Y. Kobayashi and T. Kawai, *J. Am. Chem. Soc.*, 2009, **131**, 10342–10343.

22 A. Ben-Moshe, A. O. Govorov and G. Markovich, *Angew. Chem., Int. Ed.*, 2013, **52**, 1275–1279.

23 A. S. Baimuratov, I. D. Rukhlenko, Y. K. Gun'ko, A. V. Baranov and A. V. Fedorov, *Nano Lett.*, 2015, **15**, 1710–1715.

24 F. Purcell-Milton, A. K. Visheratina, V. A. Kuznetsova, A. Ryan, A. O. Orlova and Y. K. Gun'ko, *ACS Nano*, 2017, **11**, 9207–9214.

25 G. Yang, M. Kazes and D. Oron, *Adv. Funct. Mater.*, 2018, **28**, 1802012.

26 E. D. Sone, E. R. Zubarev and S. I. Stupp, *Angew. Chem., Int. Ed.*, 2002, **41**, 1705–1709.

27 Y. Zhou, R. L. Marson, G. van Anders, J. Zhu, G. Ma, P. Ercius, K. Sun, B. Yeom, S. C. Glotzer and N. A. Kotov, *ACS Nano*, 2016, **10**, 3248–3256.

28 W. Feng, J.-Y. Kim, X. Wang, H. A. Calcaterra, Z. Qu, L. Meshi and N. A. Kotov, *Sci. Adv.*, 2017, **3**, e1601159.

29 X. Qiu, J. Hao, J. Li, Z. Gong, S. Li, J. Cheng, X. Lin and T. He, *Opt. Lett.*, 2019, **44**, 2256–2259.

30 Y. Shi, Z. Zhou, X. Miao, Y. J. Liu, Q. Fan, K. Wang, D. Luo and X. W. Sun, *J. Mater. Chem. C*, 2020, **8**, 1048–1053.

31 J. Hao, F. Zhao, Q. Wang, J. Lin, P. Chen, J. Li, D. Zhang, M. Chen, P. Liu, M.-H. Delville, T. He, J. Cheng and Y. Li, *Adv. Opt. Mater.*, 2021, **9**, 2101142.

32 J. Hao, J. Li, M. Chen, X. Duan, B. Xu, Y. Li, T. He, X. W. Sun, M.-H. Delville and J. Cheng, *Mater. Chem. Front.*, 2022, **6**, 1194–1208.

33 Y. Ben-Shahar and U. Banin, *Top. Curr. Chem.*, 2016, **374**, 54.

34 W. Ma, J. Mao, C. Hao, L. Xu, C. Xu and H. Kuang, *Appl. Catal., B*, 2019, **245**, 691–697.

35 T. O'Connor, M. S. Panov, A. Mereshchenko, A. N. Tarnovsky, R. Lorek, D. Perera, G. Diederich, S. Lambright, P. Moroz and M. Zamkov, *ACS Nano*, 2012, **6**, 8156–8165.

36 K. Wu, Z. Chen, H. Lv, H. Zhu, C. L. Hill and T. Lian, *J. Am. Chem. Soc.*, 2014, **136**, 7708–7716.

37 K. Wu, H. Zhu and T. Lian, *Acc. Chem. Res.*, 2015, **48**, 851–859.

38 I. Coropceanu, A. Rossinelli, J. R. Caram, F. S. Freyria and M. G. Bawendi, *ACS Nano*, 2016, **10**, 3295–3301.

39 N. G. Pavlopoulos, J. T. Dubose, Y. Liu, X. Huang, N. Pinna, M.-G. Willinger, T. Lian, K. Char and J. Pyun, *CrystEngComm*, 2017, **19**, 6443–6453.

40 D. Kim, Y. K. Lee, D. Lee, W. D. Kim, W. K. Bae and D. C. Lee, *ACS Nano*, 2017, **11**, 12461–12472.

41 L. Carbone, C. Nobile, M. De Giorgi, F. D. Sala, G. Morello, P. Pompa, M. Hytch, E. Snoeck, A. Fiore, I. R. Franchini, M. Nadasan, A. F. Silvestre, L. Chiodo, S. Kudera, R. Cingolani, R. Krahne and L. Manna, *Nano Lett.*, 2007, **7**, 2942–2950.

42 W. Zhang, M. F. Prodanov, J. Schneider, S. K. Gupta, T. Dudka, V. V. Vashchenko, A. L. Rogach and A. K. Srivastava, *Adv. Funct. Mater.*, 2019, **29**, 1805094.

43 I. Hadar, J. P. Philbin, Y. E. Panfil, S. Neyshtadt, I. Lieberman, H. Eshet, S. Lazar, E. Rabani and U. Banin, *Nano Lett.*, 2017, **17**, 2524–2531.

44 A. Polovitsyn, A. H. Khan, I. Angeloni, J. Q. Grim, J. Planelles, J. I. Clemente and I. Moreels, *ACS Photonics*, 2018, **5**(11), 4561–4568.

45 F. Pisanello, G. Leménager, L. Martiradonna, L. Carbone, S. Vezzoli, P. Desfonds, P. D. Cozzoli, J.-P. Hermier, E. Giacobino, R. Cingolani, M. De Vittorio and A. Bramati, *Adv. Mater.*, 2013, **25**, 1974–1980.

46 R. Krahne, M. Zavelani-Rossi, M. G. Lupo, L. Manna and G. Lanzani, *Appl. Phys. Lett.*, 2011, **98**, 063105.

47 E. Khon, K. Lambright, R. S. Khnayzer, P. Moroz, D. Perera, E. Butaeva, S. Lambright, F. N. Castellano and M. Zamkov, *Nano Lett.*, 2013, **13**, 2016–2023.

48 C. She, A. Demortière, E. V. Shevchenko and M. Pelton, *J. Phys. Chem. Lett.*, 2011, **2**, 1469–1475.

49 G. Menagen, D. Mocatta, A. Salant, I. Popov, D. Dorfs and U. Banin, *Chem. Mater.*, 2008, **20**, 6900–6902.

50 G. Menagen, J. E. Macdonald, Y. Shemesh, I. Popov and U. Banin, *J. Am. Chem. Soc.*, 2009, **131**, 17406–17411.

51 S. Deka, A. Quarta, M. G. Lupo, A. Falqui, S. Boninelli, C. Giannini, G. Morello, M. De Giorgi, G. Lanzani,





C. Spinella, R. Cingolani, T. Pellegrino and L. Manna, *J. Am. Chem. Soc.*, 2009, **131**, 2948–2958.

52 J. Qin, J. Hao, W. Chen, J. Deng, D. Wang, B. Xu, D. Wu, K. Wang, S. Li and Z. Wen, *SID Symp. Dig. Tech. Pap.*, 2016, **47**, 428–431.

53 Z. Zhou, K. Wang, Z. Zhang, C. Zhang, H. Liu, Y. Zhang, Z. Wen, S. Li, J. Hao, B. Xu, S. J. Pennycook, K. L. Teo and X. W. Sun, *IEEE Photonics J.*, 2019, **11**, 1–11.

54 W. W. Yu, L. Qu, W. Guo and X. Peng, *Chem. Mater.*, 2003, **15**, 2854–2860.

55 Z. A. Peng and X. Peng, *J. Am. Chem. Soc.*, 2001, **123**, 1389–1395.

56 J. A. Edgar, A. M. McDonagh and M. B. Cortie, *ACS Nano*, 2012, **6**, 1116–1125.

57 R. Viswanatha, H. Amenitsch, S. Santra, S. Sapra, S. S. Datar, Y. Zhou, S. K. Nayak, S. K. Kumar and D. D. Sarma, *J. Phys. Chem. Lett.*, 2010, **1**, 304–308.

58 H. Su, J. D. Dixon, A. Y. Wang, J. Low, J. Xu and J. Wang, *Nanoscale Res. Lett.*, 2010, **5**, 823.

59 X. Chuang, H. Hongxun, C. Wei and W. Jingkang, *J. Cryst. Growth*, 2008, **310**, 3504–3507.

60 C. R. Bullen and P. Mulvaney, *Nano Lett.*, 2004, **4**, 2303–2307.

61 B. Pan, R. He, F. Gao, D. Cui and Y. Zhang, *J. Cryst. Growth*, 2006, **286**, 318–323.

62 X. Chen, J. Wang, R. Pan, S. Roth and S. Förster, *J. Phys. Chem. C*, 2021, **125**, 1087–1095.

63 W. Chen, K. Wang, J. Hao, D. Wu, J. Qin, D. Dong, J. Deng, Y. Li, Y. Chen and W. Cao, *Nanophotonics*, 2016, **5**, 565–572.

64 G. Bertoni, V. Grillo, R. Brescia, X. Ke, S. Bals, A. Catellani, H. Li and L. Manna, *ACS Nano*, 2012, **6**, 6453–6461.

65 K. Wu, L. J. Hill, J. Chen, J. R. McBride, N. G. Pavlopoulos, N. E. Richey, J. Pyun and T. Lian, *ACS Nano*, 2015, **9**, 4591–4599.

66 B. T. Diroll, N. Gogotsi and C. B. Murray, *Chem. Mater.*, 2016, **28**, 3345–3351.

67 S. Christodoulou, F. Rajadell, A. Casu, G. Vaccaro, J. Q. Grim, A. Genovese, L. Manna, J. I. Clemente, F. Meinardi, G. Rainò, T. Stöferle, R. F. Mahrt, J. Planelles, S. Brovelli and I. Moreels, *Nat. Commun.*, 2015, **6**, 7905.

68 G. G. Yordanov, C. D. Dushkin, G. D. Gicheva, B. H. Bochev and E. Adachi, *Colloid Polym. Sci.*, 2005, **284**, 229–232.

69 G. G. Yordanov, E. Adachi and C. D. Dushkin, *Colloids Surf. A*, 2006, **289**, 118–125.

70 J. Cheng, E. H. Hill, Y. Zheng, T. He and Y. Liu, *Mater. Chem. Front.*, 2018, **2**, 662–678.

71 S. Deka, A. Falqui, G. Bertoni, C. Sangregorio, G. Poneti, G. Morello, M. D. Giorgi, C. Giannini, R. Cingolani, L. Manna and P. D. Cozzoli, *J. Am. Chem. Soc.*, 2009, **131**, 12817–12828.

72 D. V. Talapin, J. H. Nelson, E. V. Shevchenko, S. Aloni, B. Sadtler and A. P. Alivisatos, *Nano Lett.*, 2007, **7**, 2951–2959.

73 J. J. Li, Y. A. Wang, W. Guo, J. C. Keay, T. D. Mishima, M. B. Johnson and X. Peng, *J. Am. Chem. Soc.*, 2003, **125**, 12567–12575.

74 X. Wang, J. Hao, J. Cheng, J. Li, J. Miao, R. Li, Y. Li, J. Li, Y. Liu, X. Zhu, Y. Liu, X. W. Sun, Z. Tang, M.-H. Delville, T. He and R. Chen, *Nanoscale*, 2019, **11**, 9327–9334.

75 J. K. Choi, B. E. Haynie, U. Tohgha, L. Pap, K. W. Elliott, B. M. Leonard, S. V. Dzyuba, K. Varga, J. Kubelka and M. Balaz, *ACS Nano*, 2016, **10**, 3809–3815.

76 M. Puri and V. E. Ferry, *ACS Nano*, 2017, **11**, 12240–12246.

77 I. V. Martynenko, A. S. Baimuratov, V. A. Osipova, V. A. Kuznetsova, F. Purcell-Milton, I. D. Rukhlenko, A. V. Fedorov, Y. K. Gun'ko, U. Resch-Genger and A. V. Baranov, *Chem. Mater.*, 2018, **30**, 465–471.

78 X. Gao, X. Zhang, K. Deng, B. Han, L. Zhao, M. Wu, L. Shi, J. Lv and Z. Tang, *J. Am. Chem. Soc.*, 2017, **139**, 8734–8739.

79 V. Kuznetsova, Y. Gromova, M. Martinez-Carmona, F. Purcell-Milton, E. Ushakova, S. Cherevkov, V. Maslov and Y. K. Gun'ko, *Nanophotonics*, 2021, **10**, 797–824.